nature communications

Article

https://doi.org/10.1038/s41467-025-67817-y

Designer RNA nanostructures co-transcribed and self-assembled inside human cell nuclei

Received: 5 June 2025

Accepted: 9 December 2025

Xu Chang[1,4], Maciej Jeziorek[2,4], Qi Yang[1], Edward M. Bonder[2], Hao Yan[3], Jean-Pierre Etchegaray[2] & Fei Zhang[1]

The use of nucleic acid-based nanostructures as synthetic biological tools to interface with and regulate cell processes remains challenging. A major obstacle lies in nuclear delivery and retention within live eukaryotic cells. Here, we present a platform of single-stranded RNAs that can co-transcriptionally fold into defined nanostructures and assemble into rings, ribbons, and nanonet-like architectures. We validate the formation of these structures in vitro using atomic force microscopy. Then, we demonstrate the functional integration of fluorescent aptamers and RNA sensing capability within the single chain by co-folding with these structures. Notably, we show that the RNA nanonets can be co-transcriptionally produced and assembled directly inside the nucleus of live human cells. We use confocal live-cell imaging and transmission electron microscopy to reveal well-defined nanostructure patterns retained in the nucleus. Together, these results establish a genetically encoded, self-assembling RNA nanostructure system with programmable geometry and localization, providing a foundation for the development of RNA-based nanodevices to examine biological properties in live cells and tissues.

RNA plays essential roles in genetic regulation, catalysis, and molecular organization[1]. A critical aspect of RNA function is its subcellular localization, which is tightly regulated in living cells. Most RNA molecules, including messenger RNAs (mRNAs), are transcribed in the nucleus, undergo processing, and are subsequently exported to the cytoplasm. Other types of RNAs, such as long non-coding RNAs (lncRNAs), are often retained in the nucleus, functioning in gene regulatory programs. There are complex mechanisms controlling RNA localization that involve nuclear export signal sequences and specialized RNA structures[2,3]. Due to its complexity, understanding and potentially controlling the subcellular localization of RNA, particularly synthetic RNA nanostructures that do not occur naturally, has remained a challenge. A promising strategy is co-transcriptional folding, wherein RNA self-folds while being transcribed by RNA polymerase. This approach ensures higher fidelity and yield of desired nanostructures to be produced in large-scale, using cost-effective materials and, more importantly, allows the in vivo assembly of RNA nanostructures by directly interacting with components of living cells.

Previous works in synthetic co-transcriptional RNA design employed multiple strategies, such as antiparallel crossover[4–6], branch-kissing loops[7], and stem-loops with kissing loops[8], to create diverse RNA assemblies. These co-transcriptional folding RNA structures have been expressed and engineered to work in various environments, including *E. coli*[8], synthetic lipid membranes[6], and living cells[7–12]. However, direct visualization of the structure-defined, synthetic RNA nanostructures in living eukaryotic cells, particularly in the nucleus, has not been achieved. The ability to generate and retain synthetic co-transcriptional RNA assemblies inside the nucleus will help us understand the requirements for RNA subcellular localization as well as push forward applications in RNA-based imaging technologies, specific RNA biosensing for disease diagnosis, and new therapeutics based on simultaneous targeting of entire cellular pathways rather than single molecular components.

---

[1]Department of Chemistry, Rutgers University, Newark, NJ, USA. [2]Department of Biological Sciences, Rutgers University, Newark, NJ, USA. [3]School of Molecular Sciences and Center for Molecular Design and Biomimetics, The Biodesign Institute, Arizona State University, Tempe, AZ, USA. [4]These authors contributed equally: Xu Chang, Maciej Jeziorek. e-mail: jeanpierre.etchegaray@rutgers.edu; fei.zhang@rutgers.edu

One strategy that has shown promise in nucleic acid nanotechnology is the use of parallel crossovers, a structural feature that was initially developed in DNA nanotechnology[13,14], later adapted to RNA structures[15], and recently used to fold single-chain DNA and RNA[16–18]. This design feature enables the construction of single-stranded motifs without internal kissing loops, offering advantages in both structural stability and modular assembly.

Here, we report a systematic design strategy for the rational creation of a category of co-transcriptionally folded RNA nanostructures that assemble into nanorings, linear arrays, and extended two-dimensional lattices. The design incorporates RNA paranemic cohesion for stable secondary structure formation and terminal kissing loops for higher-order assembly. These synthetic RNA motifs are compact, modular, and able to fold during transcription both in vitro and in live human cells. By integrating light-up RNA aptamers into the designs, we enable fluorescent visualization of these nanostructures in vitro and in living human cells. Furthermore, we demonstrate that RNA arrays can function as sequence-selective sensors by integrating split aptamers to detect RNA targets in vitro. Notably, we demonstrate direct visualization of assembled RNA 2D arrays remaining inside the nuclei of human cells after transient transfection using electron microscopy. This work expands the capabilities of RNA nanotechnology and provides new routes for nuclear-localized RNA materials in biosensing, intracellular imaging, and gene regulation.

Results

Design of co-transcriptional folding RNA nanostrcutures based on paranemic cohesions

We developed a systematic design method that allowed single-stranded RNA (ssRNA) nanostructures to fold co-transcriptionally by leveraging RNA A-form parallel crossovers and terminal kissing loops (KLs) for higher-order assembly into rings, linear arrays, and lattices. A synthetic structural feature, RNA paranemic cohesion (PC), was employed in the RNA tiles to enable the continuous single-strand routing (Fig. 1A, B and Supplementary Fig. 1). For the higher-order assembly between ssRNA tiles, three types of RNA KLs were employed, including 180° RNA KLs, 120° RNA KLs, and RNA branch kissing loops (BKLs), to create a variety of assemblies (Supplementary Figs. 2 and 3). In 180° RNA KLs and 120° RNA KLs interactions, two terminal loops hybridize at angles of 180° and 120°, respectively. The BKL features an additional helix extending from one side of the terminal loop, enabling branching in the assembled structures.

To design a tile, generally, we first determined the overall structure of an RNA tile, including the number and locations of paranemic cohesions. Each RNA PC domain contains top two strands and bottom two strands, forming stable secondary structural units. RNA KLs were incorporated at the terminals not only for the single-stranded routing but also for encoding the matching rules between tiles, enabling programmable formation of lattices and arrays. Figure 1A shows an example of designing a ssRNA tile containing two PC domains and two KL domains. We planned the routing of the single-chain RNA by introducing an additional parallel crossover at the center of the tile to bridge the two helices, allowing us to connect all domains into a single continuous circular strand. Then, we chose the location of the 5′ end to initiate transcription, with the formation of stem loops, by creating a nick position on the circular strand.

After the structural design, the sequence design of a tile was conducted by following several steps. Generally, we first assigned the sequences of certain nucleotides at key locations, such as 5′ end, kissing loops, and PC domains. Then, we will generate sequences domain by domain from 5′ down to the 3′ end (steps 1 to 4 in Fig. 1C) to ensure the formation of the correct secondary structure of each stem loop and to allow these domains to further interact through paranemic cohesion to form the overall shape (detailed sequence assignment protocol in "Materials and Methods").

We designed five ssRNA tiles with different geometries and interactive motifs by varying tile length, the number and locations of crossovers, and the incorporation of KLs and BKLs, resulting in the formation of nanorings, linear arrays, and 2D lattices (Fig. 2A). In our co-transcriptional protocol, DNA template, T7 polymerase, and NTPs were added to a mica surface and assembled at 37 °C. By using this protocol, all ssRNA tiles were capable of assembling co-transcriptionally, generating well-formed structures as shown by atomic force microscopy (AFM) images. Array sizes and structural quality improved when RNA was subjected to post-transcriptional purification and controlled thermal annealing.

For the five designs, AFM revealed distinct assembly behaviors (Fig. 2B and Supplementary Fig. 4). D1 used 120° RNA KL interactions and formed hexagonal rings. D2 and D3 generated zigzag and linear arrays, mediated by 120° and 180° RNA KLs, respectively. D4 and D5, which differ in the number of paranemic cohesion domains, both produced 2D waffle-like lattices, enabled by the orthogonal arrangement of located BKLs and 180° RNA KLs. These results demonstrate the feasibility of using paranemic cohesion and kissing loops to construct structurally diverse artificial ssRNA tiles and assemblies that can fold co-transcriptionally, allowing us to create complex and functional synthetic RNA nanostructures, such as RNA tiles with defined curvature and the integration of functional aptamers.

Curved RNA tiles for nanoring assembly

Curvature is an interesting synthetic structural feature that has been demonstrated in DNA origami[19,20], showing precise control over complex nanostructures. We introduced this structural feature into our ssRNA tile system to show the robustness of our design methods. In our ssRNA tiles, each tile body comprises two continuous double-stranded RNA helices, allowing us to introduce curvature by inserting or deleting nucleotides between crossovers. To explore this strategy, we designed and characterized three curved tiles (D6 to D8) with different sizes, bending, and routings (Fig. 2C). D6 and D8 have the same overall length with 11 nt deletion in the bottom helix relative to the top helix, generating asymmetry that introduces curvature. The only difference between them lies in the position of the central crossover. D7 shares the same crossover position as D6 but features longer helical segments between the two PC domains: the upper helix spans 4.5 turns and the lower helix spans 3.5 turns, compared to D6, which has 3.5 turns and 2.5 turns, respectively. AFM images revealed that all three curved tiles successfully assembled into nanorings, confirming that the engineered curvature was sufficient to induce ring formation (Supplementary Figs. 18–23). To compare their assembly behavior quantitatively, we measured the diameters of the resulting nanorings and fitted their distribution curves (Fig. 2D). D8 produced rings with diameters closest to those expected for a pentamer ring, consistent with the angular contribution of the 11nt deletion. D6 formed rings with smaller diameters, indicating tetrameric or smaller assemblies, potentially due to the specific placement of its crossover. D7 showed a broader size distribution, likely reflecting the increased flexibility of the longer RNA helices in this design.

Although RNA kissing loops have been well-characterized in various biological and synthetic contexts, their behavior within co-transcriptionally folded ssRNA nanostructures, particularly their sensitivity to buffer conditions relative to tile stability and higher-order assemblies, remains less well understood[21]. Having successfully designed ssRNA tiles with curvature that assemble into nanorings, we leveraged these finite-sized architectures to study the intermolecular interaction of 180° RNA kissing loops under varying ionic conditions. Our parallel crossover-based ssRNA structures are uniquely well-suited for this investigation because the individual tiles contain no internal KLs, and the KLs are used exclusively at the termini for intermolecular assembly. Therefore, any changes in KL interactions affect only the

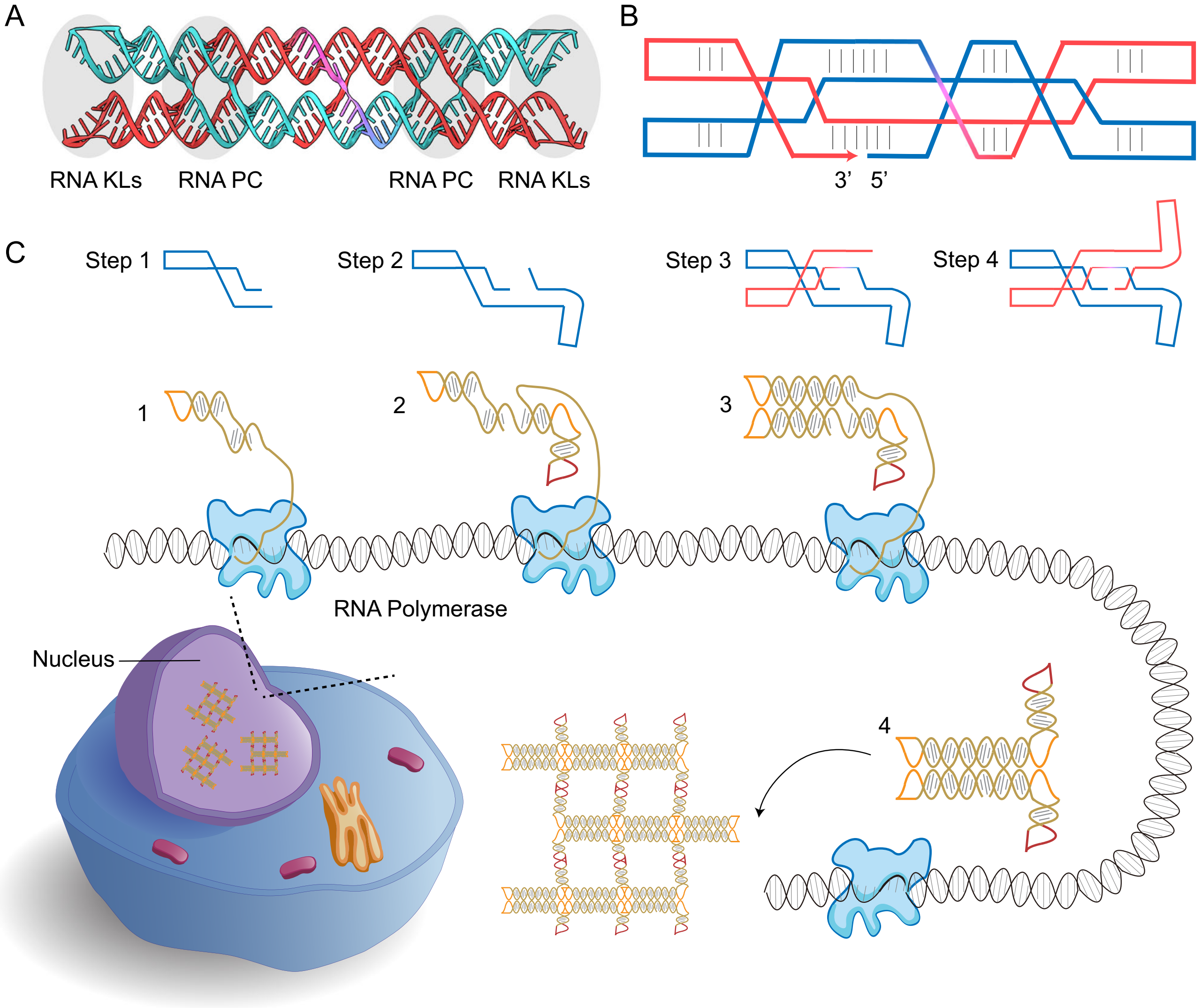

Fig. 1 | Design, folding, and cellular assembly of co-transcriptionally folded ssRNA tiles. A Schematic design of a ssRNA tile, Design 3 (D3). 'RNA KLs' refers to RNA kissing loop motifs, and 'RNA PC' denotes RNA paranemic cohesion. The 3D model shows the composition and folded conformation of the ssRNA tile. **B** Routing map of the co-transcriptional folding of D3. The blue line indicates the first half of the D3 sequence, and the red line indicates the second half. **C** Schematic of the co-transcriptional folding and assembly of Design 4 (D4) tile in the human cell nucleus. Step 1: RNA polymerase binds the DNA template and begins synthesizing the first paranemic cohesion domain, leaving an open stem-loop structure. Step 2: The first half of D4 is completed, forming half of the RNA PC domain and one branched arm containing an RNA branch kissing loop (BKL). Step 3: The second half of the RNA PC domain is synthesized and pairs with the first half, forming a stabilized RNA PC configuration. Step 4: The second branched arm with an RNA BKL is transcribed, completing the folding of D4. Tile monomers subsequently assemble into lattices within the nucleus via RNA kissing loop interactions.

nanoring formation, without compromising the structural integrity of individual ssRNA tiles.

We first test directly annealed D8 samples in a set of TA buffers containing 0, 0.5, 1, 2, 4, or 6 mM Mg^{2+}. The nanoring formation started to be observed when the Mg^{2+} concentration reached 0.5 mM or higher (Supplementary Figs. 25–27). Notably, D8 monomers folded into the target tile shape with some level of deformations even under 0 mM Mg^{2+}, as confirmed by AFM imaging, indicating that individual ssRNA tiles can fold across a broad range of ionic buffer conditions. This data aligns with the previous report that ssRNA origami based on paranemic cohesion can be stably stored in phosphate-buffered saline (PBS) without the addition of Mg cations for months, remaining intact[22]. In addition, KL-mediated ring formation required elevated Mg^{2+} levels, suggesting that KL interactions for higher-order assembly are sensitive to ionic strength. Similar results were also reported in a previous study[21], where stem-looped KL tiles were used to study their assembly under 0, 1, and 5 nM of Mg^{2+}, and the results showed that conformation of the higher-order RNA assemblies can be stabilized by the addition of magnesium.

Integration of fluorescence aptamers into RNA assemblies

To introduce the functionality of ssRNA tiles and facilitate their use in vivo, we incorporated fluorescent RNA aptamer sequences into the tile designs. Specifically, we used the Broccoli aptamer and a split Broccoli aptamer, both of which enhance the fluorescence of small-molecule dye DFHBI-1T[23,24]. To preserve the co-transcriptional folding and structural integrity of the tiles, we tested four designs, D9 to D12, with different aptamer-inserting locations within the RNA tile sequences that were based on the previously validated D3 and D4 tile frameworks (Fig. 3A–C). Each design employed a different strategy for aptamer integration. D9 had an aptamer tagged at the 3' end of the tile sequence. D10, a larger design, placed the aptamer sequence near the 3' end but internal to the strand. D11 displayed the aptamer as an extension from a kissing loop, while D12 incorporated the split

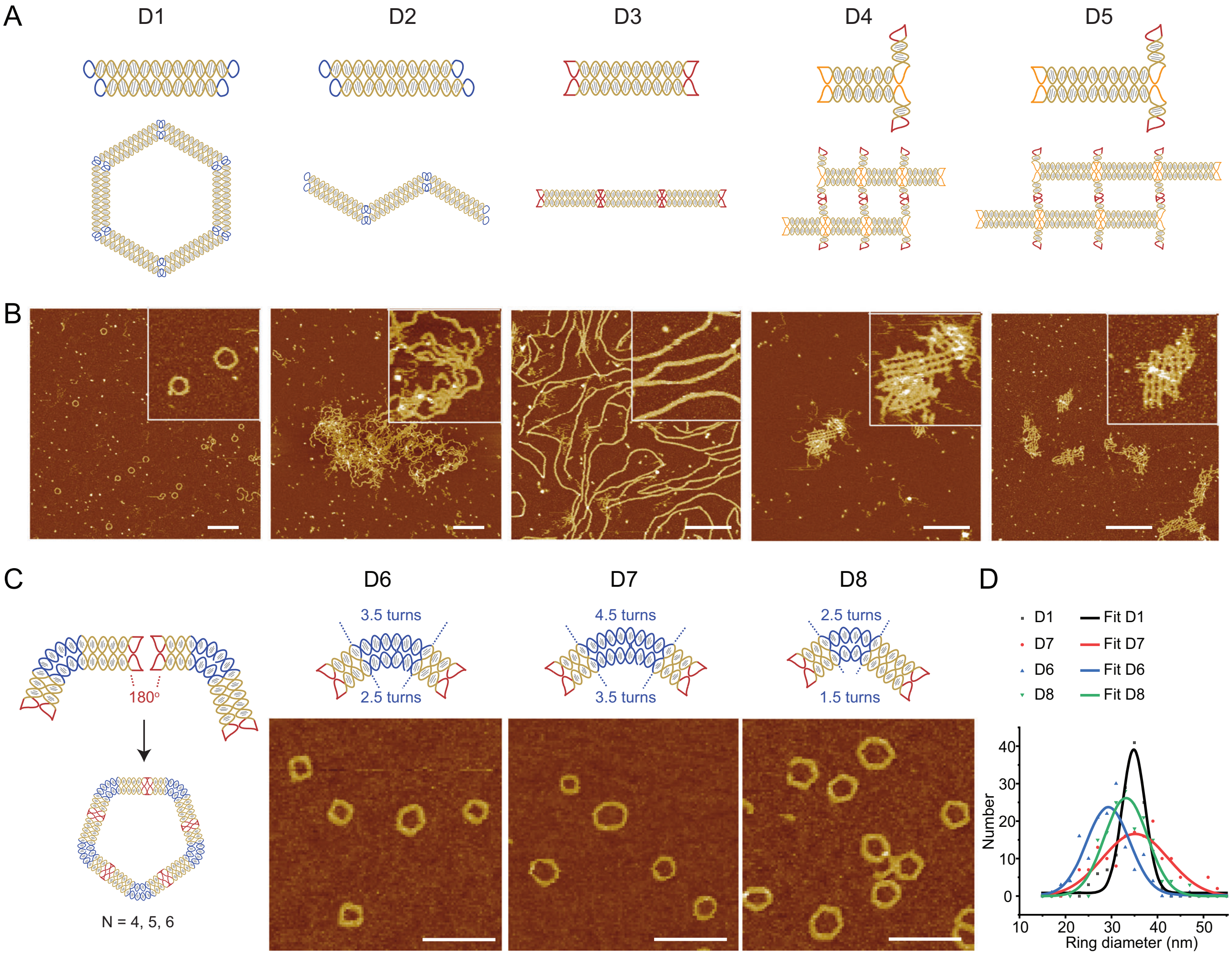

Fig. 2 | Programming ssRNA tiles to assemble into arrays and finite-sized nanorings. **A** Schematics of Design 1 to 5 (D1-D5) and their intended assemblies. **B** AFM images of D1 to D5 assemblies under co-transcriptional folding. D1 forms hexamer rings. D2 generates zigzagged 1D arrays using 120° RNA KLs. D3 forms linear 1D arrays mediated by 180° RNA KLs. Both D4 and D5 assemble into waffle-like 2D lattices. However, D5 contains two paranemic cohesion domains and thus forms larger unit cells than D4, which contains only one. Scale bar: 200 nm; inset images: 200 × 200 nm. Each experiment was repeated independently three times with similar results. **C** Designing ssRNA tiles with intrinsic curvature. The schematic shows how curved tile D8 assembles into nanorings (*N* = 4, 5, or 6 monomers) through 180° KL interactions. In these designs, the inner RNA helix is shorter than the outer helix by one helical turn (colored navy). Specifically, D6 has 3.5 turns in the upper helix and 2.5 turns in the lower helix; D7 has 4.5 turns in the upper helix and 3.5 turns in the lower helix. Compared to D6 and D7, D8 has no additional crossover between helices and features 2.5 turns in the upper helix and 1.5 turns in the lower helix. Scale bar for AFM images: 100 nm. **D** Statistical analysis of ring diameter distributions. Diameters of rings assembled from D6, D7, D8, and D1 were measured and plotted to compare size variations. Gaussian fitting was applied. D1 forms hexamer rings by relying on 120° KLs, not structural curvature.

Broccoli sequence separately at 5′ and 3′ ends. These designs were optimized to maintain robustness during folding while accommodating the aptamer sequences at different locations. All four designs were transcribed and assembled directly without purification and annealing. AFM imaging confirmed the successful formation of the intended assemblies for all four designs (Fig. 3C and Supplementary Fig. 29). D9 and D10 formed 2D lattices, while D11 and D12 assembled into linear arrays. Fluorescent measurements after 1 h of transcription revealed that D9 and D12 produced stronger signals than D10 and D11 (Fig. 3B), indicating possible preferred terminal locations for integrating aptamer sequences.

Scaffolded RNA sensors based on split aptamers

To explore the sensing applications of ssRNA tiles in vitro, we designed D13, a tile incorporating a split Broccoli aptamer and a target-responsive domain for RNA detection. RNA sensing is a useful approach for disease diagnostics and gene expression studies[25,26]. We chose a target sequence derived from the KRAS Proto-Oncogene GTPase, a known biomarker for multiple cancer types with a higher impact on pancreatic and colorectal cancers[27,28]. Inspired by our previous study, that multistranded RNA tiles can incorporate a split Broccoli aptamer and a target-responsive domain for RNA sensing[29], we present a ssRNA tile D13 to explore the sensing application in vitro. As shown in Fig. 3B, D13 consists of two RNA helices connected by a single crossover, where one helix features two 180° KLs at both ends and the other helix is capped with two T-junction loops. The target-sensing domain is split across the 5′ and 3′ ends of the tile, flanking the split Broccoli aptamer. Upon hybridization with the target RNA, the complementary sensing regions bring together the split aptamer fragments, reconstituting the aptamer core and activating fluorescence in the presence of DFHBI-1T (Supplementary Fig. 28). AFM images showed the co-transcriptionally assembled D13, with unpaired sensing domains hanging out from the tile body (Supplementary Fig. 40).

To evaluate sensing performance, we measured the dose-response curve of D13 against increasing concentrations of the

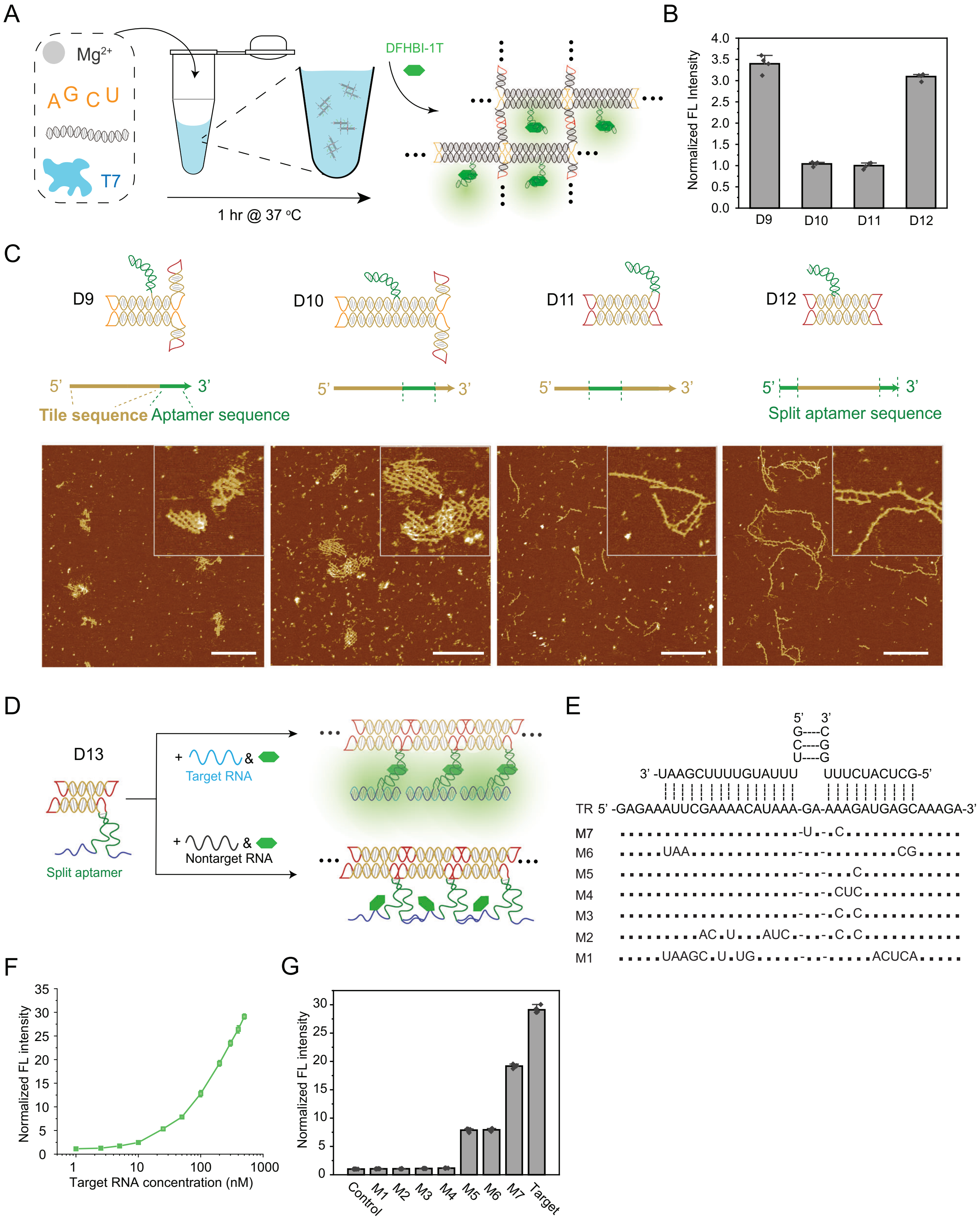

target RNA (Fig. 3D). A significant increase in fluorescence was observed between 5 and 10 nM target RNA, indicating a low detection threshold. We also tested the dye response curve in the presence of both ssRNA tiles and target RNA, and the RNA target response curve with ssRNA tiles and dye present (Supplementary Fig. 44). Both experiments were performed in a one-pot, co-transcriptional system without any purification or annealing, demonstrating the sensor's compatibility with rapid, scalable workflows. In addition to sensitivity, we assessed the specificity of D13 by testing various mutated RNA targets, M1 to M7, that were derived from a previous work[29]. M1 to M4 contained 12nt, 8nt, 2nt, and 3nt substitutions, respectively, and produced fluorescence levels comparable to the negative control. M5 to M7, with 1nt, 5nt, and 2nt mutations, generated reduced but still detectable signals relative to the fully matched target (Fig. 3E–G and

Fig. 3 | Functional assembly of light-up ssRNA arrays and sensors by incorporating RNA aptamers. A Schematics illustrate the synthesis, assembly, and fluorescence activation of D10. D10 is a ssRNA array embedded with fluorescence aptamers. **B** Fluorescence measurements of D9 to D12 after transcription from (**A**). All samples were tested after the same transcription time without additional purification or annealing. **C** Models, routing maps, and AFM images of D9 to D12. In our design, D9 to D12 represent different methods for inserting aptamer sequences for comparison. D9: RNA Broccoli aptamer appended to the 3′ end. D10: Broccoli aptamer embedded internally, near the 3′ end. D11: Broccoli aptamer inserted into the middle of the strand, forming part of a branch kissing loop (BKL). D12: Broccoli aptamer split into two halves, with the first half at the 5′ end and the second half at the 3′ end. D9 and D10 assemble into 2D lattices, while D11 and D12 form linear arrays. AFM images of aptamer lattices and arrays assembled via co-transcriptional protocols. Arrows in the AFM images of D11 and D12 indicate alternating aptamer positioning along the linear arrays. Scale bar: 300 nm; inset size: 300 × 300 nm. **D** Schematics of D13 as an RNA sensor. **E** Schematics of the sensing domain of D13 hybridized with target RNA and the sequences of each mutation. **F** Sensitivity testing of D13 for target RNA detection. **G** Specificity testing of Co-APT V5 against RNA targets with different mutation numbers and locations. Fluorescence intensity data are reported as means ± standard errors (SE) from $n = 6$ experiments.

Supplementary Fig. 45). This partial activation likely results from the specific locations or minimal number of mismatches, which may permit partial hybridization to facilitate the aptamer core formation, suggesting that the specificity of our sensor is also influenced by structural factors of the split aptamer in addition to the number of mismatches. Although the current sensing experiments are conducted in a cell-free synthetic system, previous studies of RNA biosensing using split Broccoli[30,31] suggest that this sensor design potentially can also be adapted in living cells for visualizing and monitoring RNA assembly.

Folding and assemble RNA structures in human cell nuclei

Building upon the in vitro characterization, we next assessed whether our designs could be applied in biologically relevant settings. We selected D4 and D10, forming large nanonet-like configurations (Figs. 2A D4 and 3B D10) to generate expression plasmids (Supplementary Figs. 72–74) and evaluate their co-transcription and in vivo assembly by transfecting human embryonic kidney 293FT cells (HEK293FT) (Fig. 4A). Their expression was analyzed by quantitative Reverse Transcription-PCR (RT-qPCR) and the nanostructures were visualized by confocal imaging. Prominent expression of both RNA structures was observed 24 h after transfection (Fig. 4B and Supplementary Fig. 46). Since most of the RNA tiles form double-stranded RNA helices upon folding, we used monoclonal J2 antibodies, which detect double-stranded RNA helices larger than 40 bp irrespective of the sequence[32]. These antibodies are widely used for detecting double-stranded RNA of viruses in infected cells[33]. To monitor transfection efficiency, we co-transfected HEK293FT cells with the D4 and D10 expression plasmids along with a plasmid expressing mCherry as a transfection marker, followed by immunostaining with J2 monoclonal antibodies. At 24 h post-transfection, we observed 68.50% and 67.09% of cells expressing mCherry showed assembled D4 and D10, respectively (Supplementary Fig. 69). We analyzed the subcellular distribution of these assemblies, classifying them as nucleus only, nucleus and cytosol, or cytosol only. For D4, 48.97 % of cells showed nuclear distribution, 47.59% showed both nuclear and cytosolic, and 3.59 % showed cytosolic only localization (Supplementary Fig. 70). For D10, 3.59% showed nucleus only, 88.11% showed nuclear and cytosolic distribution, and 11.15% cytosolic only (Supplementary Fig. 71). Notably, our assemblies localize primarily within the nuclear compartment and we observe distinct dsRNA-positive structures in most cells transfected with either D4 or D10 (Fig. 4C Top left panels, Supplementary Figs. 47 and 48). Both of these nanostructures displayed the expected nanonet-like configuration (Fig. 4C Top right panels, Supplementary Fig. 49 and 50). To further validate the structural assembly, we co-transfected cells with D4, which contains a Broccoli aptamer, and performed live-cell imaging 24 h post-transfection in the presence of DFHBI-1T and Hoechst. These live imaging studies revealed a similar nuclear nanonet-like configuration (Fig. 4C, Bottom panels, Supplementary Figs. 51–54) to the nanostructures observed in immunostained cells using J2 monoclonal antibodies (Fig. 4C, Top panels). To probe for the dynamic properties of the assembled nanostructures, we leveraged the photochemical sensitivity of the DFHBI-1T fluorophore. DFHBI-1T has been shown to undergo rapid isomerization and dissociation from the Broccoli aptamer upon laser illumination[34]. We therefore performed live-cell photobleaching experiments and observed rapid loss of fluorescent signal within the photobleached region, followed by recovery within 30 seconds (Supplementary Figs. 55 and 56). The observed nanostructures further support the dynamic binding of DFHBI-1T to correctly folded RNA tiles. Collectively, these results validate the co-transcriptional expression and proper self-assembly of our designed RNA tiles within the nucleus of human cells.

Given the resolution limits of confocal microscopy and the nanoscale dimensions of the RNA tile subunits, we sought to further characterize their assembly in HEK293 cells by performing Transmission Electron Microscopy (TEM) on the two selected tiles, D4 and D10 (Fig. 4C, Top panels). TEM analysis revealed large organized synthetic nanostructures with architectural assembly patterns that are consistent with the ones observed by immunofluorescence (Fig. 5A–C and Supplementary Figs. 57–66). We observed distinct waffle-like 2D arrays (Fig. 5B inset 5, Fig. 5C inset 7) that closely resemble those formed by co-transcriptional folding using T7 RNA polymerase visualized by AFM (Figs. 2B D4 and 3B D10). Side-by-side comparisons between AFM and TEM images at the same scale showed that D4 and D10 can efficiently assemble into nanonet-like structures both in vitro and in vivo, inside human cell nuclei. This was further demonstrated by the similar distances measured between the neighboring lines of these arrays in the AFM and TEM images (Supplementary Figs. 67).

Collectively, using both fluorescence cell imaging and TEM, D4 and D10 exhibit a co-transcriptional self-folding into a nanonet-like configuration inside human cell nuclei, with a striking similarity to the in vitro nanostructure demonstrated by AFM. Our TEM images show the integrity of nuclear components in D4-transfected HEK293 cells. For instance, the TEM shows clear nucleolar structures along with well-defined heterochromatin and euchromatin regions (Supplementary Figs. 59–61). Thus, we present a clear demonstration, both in vitro and in vivo, that our designed synthetic RNA nanonet-like structure is co-transcriptionally folded within human cells and is more prominently visible in the nucleus.

Discussion

In summary, we present a design framework for single-stranded RNA tiles that fold co-transcriptionally through paranemic cohesion domains and further assemble into defined rings, 1D, and 2D arrays. We incorporated light-up aptamers using different insertion strategies and validated their generated fluorescent signal upon transcription. In addition, we engineered one of the ssRNA tiles, D13, to contain an array of split aptamer sensors that can respond to target RNA with nanomolar sensitivity and sequence discrimination.

Particularly, our in vivo study demonstrates that two ssRNA designs, D4 and D10, that assemble into 2D arrays, primarily localize within the nuclear compartment in human cells, suggesting de novo designed, co-transcriptionally folded RNA structures can have their preferred intracellular localization. For natural RNA molecules, a key determinant of nuclear retention is the presence or absence of nuclear export signals. Protein-coding mRNAs contain sequence elements that recruit the transcription-export complex to facilitate their transport

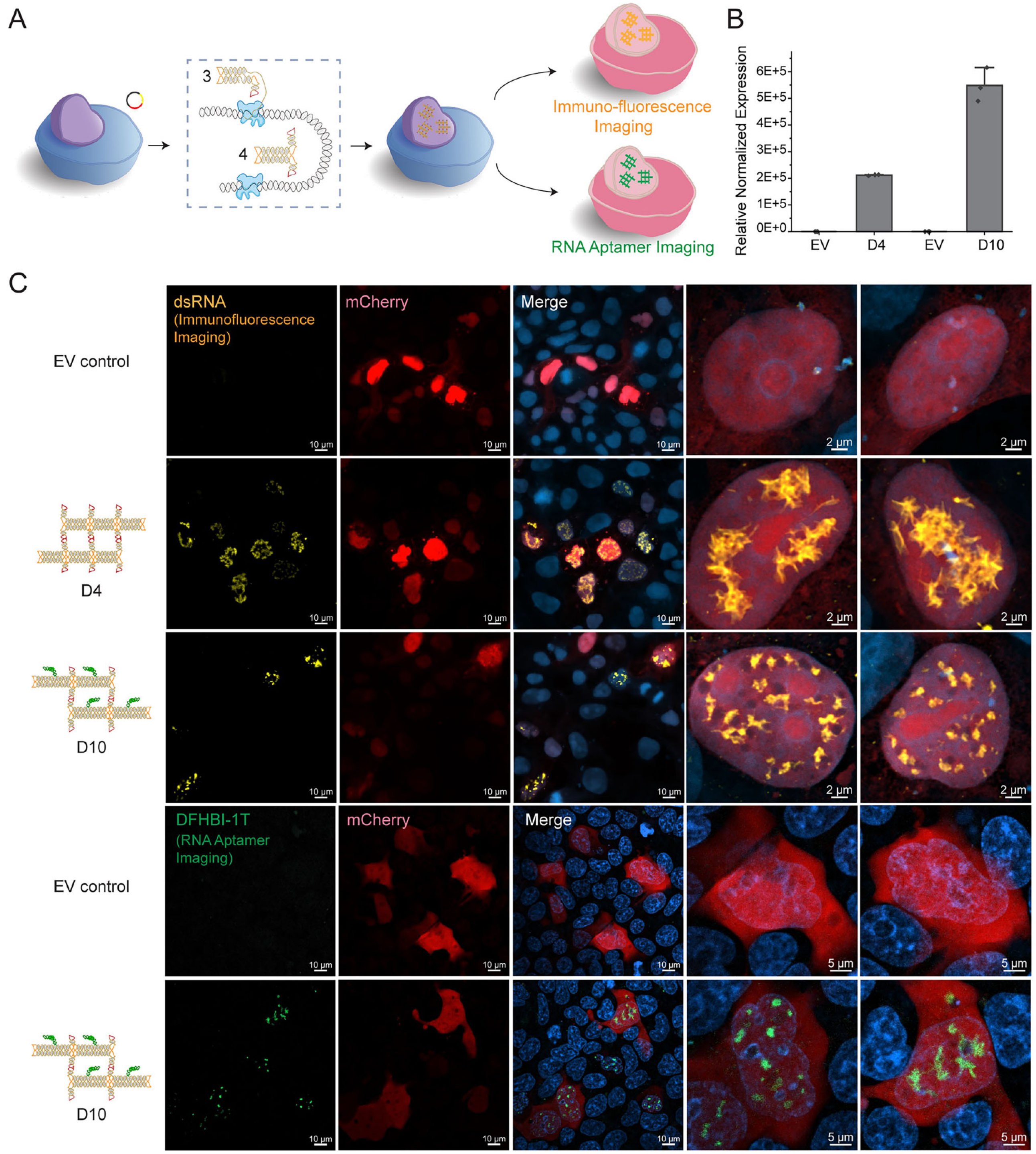

Fig. 4 | Expression and co-transcriptional folding of D4 and D10 RNA structures in mammalian cells. A Schematic of the experimental workflow. Cells are transfected with a plasmid encoding the RNA tile along with an mCherry expression vector as a transcriptional marker for 24 h. In the nucleus, the RNA co-transcriptionally assembles into large nanostructures. Assembly is visualized by confocal microscopy using the J2 antibody, which detects double-stranded RNA helices longer than 40 bp, and by live-cell imaging of the DFHBI-1T fluorophore bound to the Broccoli aptamer. **B** Quantification of RNA expression levels 24 h post-transfection by real-time qPCR using primers specific to D4 and D10 RNA structures. Relative expression levels are presented as a mean ± SEM of three technical replicates. The experiment was repeated three times independently with similar results. **C** The top three panels: co-transcriptional assembly of D4 and D10, detected by immunofluorescence with J2 antibody. High-magnification images show nuclear localization and structure of D4 and D10 assemblies by J2 staining. The bottom two panels: visualization of D10 live-cell assembly via DFHBI-1T binding to the Broccoli aptamer. High-magnification live-cell images show Broccoli-tagged D10 RNA nanostructures within the nucleus.

through nuclear pores[35]. In contrast, many nuclear-retained lncRNAs lack sequence-based export signals. Instead, previous studies have suggested that natural lncRNAs often adopt highly structured conformations, which favor interactions with nuclear proteins involved in genomic and epigenomic regulation, impeding their nuclear export[36,37]. For the synthetic RNA nanostructures, the published example of expressing branch-KL-based RNA assemblies in living cells has shown their RNA predominantly in the cytoplasm[12], potentially due

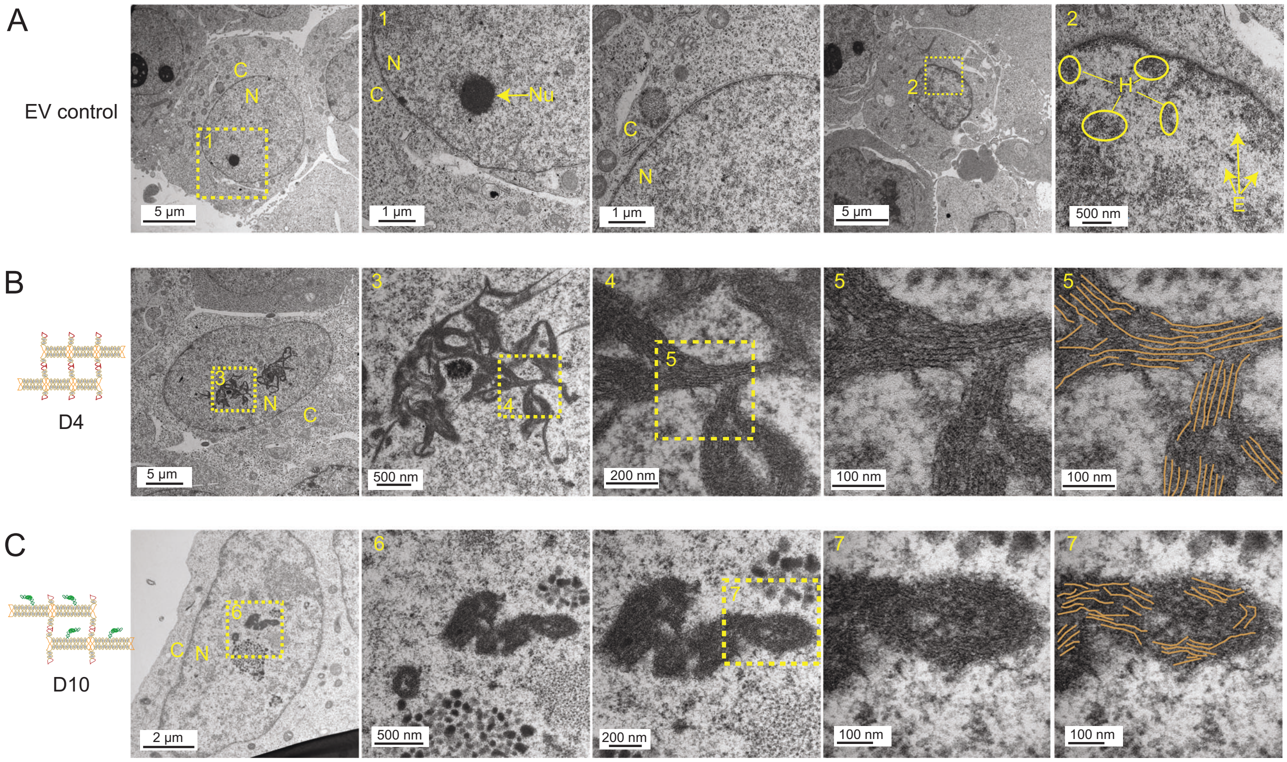

Fig. 5 | Transmission Electron Microscopy (TEM) of D4 and D10 RNA structure assembly in mammalian cells. Representative TEM images of transfected cells showing: **A** Empty vector control, **B** D4 structure, and **C** D10 structure at increasing magnifications. The images represent preparations of two samples with similar results. Major cellular structures are labeled as follows: C – cytosol, N – nucleus, Nu – nucleolus, H – heterochromatin, E – euchromatin. Insets 5 and 7 show the interpretation of array assembly patterns, with outlines indicating the structural organization of the RNA tiles.

to the initial formation of loose secondary structures that allow for export before higher-order assembly. In our work, the HEK293 cells engineered to express either D4 or D10 through transient transfections form stable, large net-like structure assemblies in nuclei. These ssRNA tiles may be produced rapidly to form large assemblies, and the ones that are too large and/or too structured to undergo nuclear export. But the factors influencing the localization of these RNA structures require comprehensive investigation in future studies. Possible considerations include structural factors (e.g., size, geometry), sequence design, the transfection method, and other parameters affecting nuclear trafficking processes.

Our findings suggest that RNA structure and folding dynamics may play a crucial role in RNA localization. This has important implications for the design of synthetic RNA nanostructures intended for nuclear applications, such as RNA-based biosensors, gene regulatory systems, or nuclear scaffolding materials. Future work will focus on elucidating the exact mechanisms governing nuclear retention, including potential interactions between our RNA assemblies and nuclear retention factors. Additionally, we project the use of these nanostructures as biosensors in live human cells and tissues capable of functioning as biosensing nanosponges that light up upon specific binding to a multitude of microRNAs, whose upregulation is detected in various diseases, including cancer.

Intriguingly, our RNA nanostructures can be viewed as mesh-like assemblies, which, based on size and general shape, resemble a synthetic version of the nuclear matrix, providing support and organization to the cell nucleus. The nuclear matrix functions as a structural framework involved in organizing the 3D genome, influencing chromatin structure and its ability to interact with transcription regulatory complexes, which consequently affect gene expression and cell physiology[38]. For future studies, we will design structural configurations with specific domains that link the 3D genome with Lamins, which are nuclear matrix proteins known to dynamically change gene expression by modifying the structure of the 3D genome known as Lamin-associated domains (LADs)[39]. This will enable us to investigate the functional impact of RNA-based nanonets, which can be used as inducible “synthetic LADs” to modulate 3D chromatin arrangements and gene expression profiles, thereby affecting cell function.

Overall, this study not only introduces a structural approach for co-transcriptionally assembled RNA nanostructures but also reveals a previously unreported RNA nuclear localization and retention property. Our work highlights the potential for engineering synthetic RNA localization mechanisms through structural design, opening new directions in RNA nanotechnology and synthetic biology.

Methods

Structural design of RNA tiles

RNA helices were created in Tiamat[40] using the Create Strand function. Helices were rotated and transferred to preferred positions where parallel crossover could be added manually. The number of nucleotides at the paranemic cohesion (PC) should be 8, and at least one turn (11nt) was used to space between neighboring PCs. Take D3 as an example, we built two paranemic cohesions with an 8 nt length. Between two paranemic cohesions, we made a center parallel crossover to route this RNA tile into a single strand. The distance between this crossover and the two paranemic cohesions was 11 nt and 14 nt to increase the stability of RNA tiles. The space between PC and kissing loop was chosen at 8 nt to increase the stability of the structure. 180° RNA kissing loops were derived from natural HIV RNA (PDB_ID: 1B8R)[41] and 120° RNA kissing loops originated from ColEI plasmid from *Escherichia coli* (PDB_ID: 2BJ2)[42]. RNA branch kissing loops originated from this published research[7]. RNA tiles were drawn in Adobe Illustrator and arrays were built by moving monomers together. Molecular models were rendered by UCSF Chimerax[43] in Fig. 1A.

Sequence assignment of RNA tiles

First, we make the first two nucleotides at 5′ GG to facilitate the RNA transcription. Then we add the sequence to the kissing loops. The total number of G and C bases in every kissing loop is 3. Next, we assign the sequence of PC domains. 4 out of 8 nt at PC are assigned G or C to increase the stability of cohesion. Then we assigned the rest of the RNA tile by the Generate Sequence function of Tiamat with the following settings: Unique Sequence Limit 4; Repetition Limit 4; G repetition Limit 3; G-C Percentage 0.5; Check Sliding Base Yes; Operation Time Out 8. Then G-U wobble pairs were added every 8 to 11 base pairs except for the paranemic cohesion and kissing loop region. After this, we break the tile into domains containing half of a paranemic cohesion and steps in the order of transcription (step 1 in Fig. 1C). NUPACK[44] and mFold[45] are used to predict the secondary structures of the half paranemic cohesion domain. If the predicted structure differs from the one we designed, we modify the nucleotides near the unexpected secondary structures until NUPACK and mFold output the correct secondary structures. This step ensures that the domain of step 1 of our tile can fold correctly during transcription. Then, we proceed to the step 2 domain (Fig. 1C) and repeat this process until both software outputs the correct folding of our structure at step 4.

Preparation of ssRNA

The subsequent RNA sequences were translated to DNA templates. T7 promoters and PCR primers were added to the 5′ and 3′ (sequence can be found in the Sequence section of this document) and ordered as gBlock DNA from Integrated DNA Technologies (IDT). The gBlock DNA was then diluted to 4 ng/μL in water and amplified by PCR with *Taq* PCR Kit, from New England Biolabs (NEB). The sample was denatured for 1 min at 95 °C, followed by 25 cycles at 95 °C for 30 s, 50 °C for 1 min, and 70 °C for 2 min. The final extension was at 70 °C for 5 min. PCR product was subjected to denaturing polyacrylamide gel purification and used for RNA transcription with the HiScribe® T7 High Yield RNA Synthesis Kit (NEB) using its protocol. RNA product was then subjected to another round of denature polyacrylamide gel purification before use.

Co-transcriptional assembly protocol

Co-transcriptional assembly was performed on mica, unless otherwise noted. A freshly peeled mica (Ted Pella) was stuck on a metal disk and was placed in a petri dish with wet filter paper to reduce humidity. This petri dish was kept at 37 °C in a PCR chamber with 80 μL of 1× TAE Mg buffer (40 mM Tris base, 20 mM acetic acid, 12.5 mM magnesium acetate, and 1 mM EDTA, with a pH of 8.2) added to the mica. A 20 μL sample was made with 30 ng DNA template, 0.01 μL T7 enzyme, 8 μL NTPs, 1 μL DTT, and 1× TAE Mg buffer instead of T7 buffer. All ingredients are from the T7 kit if otherwise noted. This sample was then transferred to the warm mica and allowed to cool stepwise from 37 °C to 20 °C over 2 h. D14 and D6 to D8 were co-transcriptionally assembled in solution in a 20 μL sample system with 30 ng DNA template, 1 μL T7 enzyme, 8 μL NTPs, 1 μL DTT, and 1× TAE Mg buffer at 37 °C for 2 hrs.

Annealing assembly protocol

Purified RNA was annealed on mica if not specifically noted. For assembly on mica, the mica preparation process was the same as the co-transcriptional protocol. After preparation, the petri dish was placed in a PCR chamber at 70 °C with 100 μL of 1× TAE Mg buffer. Prior to assembly, the RNA underwent a quick heating-cooling process (90 °C for 3 min, 4 °C for 5 min). Then, 500 ng of RNA was diluted in 20 μL of TAE Mg buffer and heated to 70 °C before being added to the warm mica. This sample underwent a stepwise cooling ramp from 70 °C to 20 °C overnight (~12 h). D14 and D6 to D8 were annealed and assembled in solution in a 20 μL sample system with 500 ng of RNA diluted in 20 μL of TAE Mg buffer, and underwent a stepwise cooling ramp from 70 °C to 20 °C overnight (~12 h).

AFM imaging

AFM imaging was carried out using Dimension FastScan AFM from Bruker in ScanAsyst in Liquid mode and ScanAsyst-Fluid+ tip from Bruker. Sample on mica was washed with 200 μL TAE Mg buffer before imaging and 2 μL 100 mM $NiCl_2$ solution was added to improve contrast. For the sample prepared in solution, 0.5 μL was diluted with TAE Mg buffer to 80 μL and mixed with 2 μL 100 mM $NiCl_2$ solution before adding to the mica. Auto controlled peak force setting was used for all samples. Ring diameter measurement in Fig. 2D of the manuscript was performed using ImageJ, and the data were processed using the Gaussian fitting function in OriginPro software.

Fluorescence measurements

Sample preparation. Experimentally, D13 was cotranscribed with HiScribe® T7 High Yield RNA Synthesis Kit (NEB) for 1 h. Then, the reaction mixture, without further purification, was directly diluted to 0.5 μM for specificity testing, and the concentration of D13 was calculated based on the OD260 reading from the Nanodrop. Noted that the in vitro transcripts always contain elongated or shortened byproducts, so that the calculated concentration is higher than the concentration of pure D13, and the accurate concentration of D13 was not quantified.

M1 to M7 are seven RNA mutants adapted from our multistranded RNA tile study[29]. Unpurified cotranscriptional products of D13 (0.5 μM) were mixed with each RNA target (0.5 μM, purified) and DFHBI-1T (10 μM), and annealed at 37 °C in a thermocycler for 30 min.

Measurement. Fluorescence signals were collected on a Horiba Fluorolog-3 spectrofluorometer with excitation at 470 nm and emission wavelengths at 505 nm. The fluorescence test of the co-transcriptional sample was performed after overnight transcription (~12 h) of the ssRNA tile using the T7 Kit protocol. A 1 μL transcription product was diluted to 50 μL in HEPES buffer containing 100 mM potassium chloride and 1 mM magnesium acetate. 1 μL 0.5 mM (Z)-4-(3,5-difluoro-4-hydroxybenzylidene)-1,2-dimethyl-1H-imidazol-5(4H)-one (DFHBI) was added before testing.

Plasmid construction

Co1-BKL and Co-APT-V2 expression plasmids were generated using standard molecular cloning techniques. Synthetic gBlocks encoding D4 and D10 (IDT) were used as templates for PCR amplification to introduce EcoRI and AgeI restriction sites. The PCR products and the pLKO.1-puro vector (Addgene #8453) was digested with EcoRI-HF and AgeI-HF (New England Biolabs) restriction enzymes and purified using the QIAquick PCR Purification Kit (Qiagen) according to the manufacturer's instructions.

The purified, digested inserts and vector were ligated using T4 DNA Ligase (NEB) at room temperature for 1 h, followed by heat inactivation at 65 °C for 20 min. Four microliters of the ligation reaction were transformed into One Shot Stbl3 chemically competent *E. coli* (Thermo Fisher Scientific) using heat shock. Colonies were screened by colony PCR using primers flanking the insertion site in the pLKO.1 vector (U6 promoter forward: 5′-CTC GAG CCG CGG CCA AAG T-3′; reverse: 5′-GAG GGC CTA TTT CCC ATG ATT CCT T-3′).

Positive clones were expanded overnight in LB medium containing ampicillin, and plasmids were isolated using the CompactPrep Plasmid Kit (Qiagen).

pLKO.1 puro was a gift from Bob Weinberg (Addgene plasmid # 8453; http://n2t.net/addgene:8453; RRID: Addgene_8453)

Cell culture and transfection

HEK293FT cells were obtained from Invitrogen (Cat# R70007) and cultured on Matrigel-coated tissue culture plates in Dulbecco's Modified Eagle Medium (DMEM; Thermo Fisher Scientific) supplemented with 10% fetal bovine serum (FBS; HyClone), 1% non-essential amino acids (NEAA; Sigma), 1% GlutaMAX (Gibco), 1% sodium pyruvate

(Sigma), and 1% penicillin-streptomycin (Gibco). Cells were maintained at 37 °C in a humidified incubator with 5% CO_2 and passaged twice per week.

For transfection experiments, cells were trypsinized the day before and plated onto Matrigel-coated coverslips (for immunofluorescence) or chambered dishes (for live imaging) at a density of 2.5×10^2 to 4.5×10^2 cells per well. On the day of transfection, 290 ng of expression plasmid and 10 ng of mCherry vector were diluted in Opti-MEM (Gibco) and mixed with polyethyleneimine (PEI) at a final DNA:PEI ratio of 1:4. The mixture was incubated for 20 min at room temperature to allow transfection complexes to form. Cells were washed and fresh antibiotic-free medium was added prior to the addition of transfection complexes. After a 6-hour incubation, the medium was replaced with fresh complete medium. Cells were either fixed or collected for downstream experiments 24 h post-transfection.

Immunofluorescence

Fixed cells were washed three times with PBS and permeabilized with 0.5% Triton X-100 (TX100) in PBS for 10 min at room temperature. To reduce non-specific binding, cells were blocked with a solution containing 2% goat serum, 1% BSA, 0.2% skim milk, 0.1 M glycine, and 0.1% TX100 in PBS for 1 h at room temperature.

Primary antibody incubation was performed overnight at 4 °C in a humidified chamber using mouse anti-dsRNA (J2 clone, Nordic-MUbio) diluted 1:250 in 0.1% BSA in PBS. The following day, the cells were washed six times by gently dipping them in a beaker containing 0.1% TX-100 in PBS. Cells were then incubated with Cy2- or Cy5-conjugated secondary antibodies (Jackson ImmunoResearch) for 1 h at room temperature in a dark, humidified chamber.

After secondary incubation, cells were washed again and mounted using Vectashield Vibrance with DAPI (Vector Laboratories). Mounted slides were allowed to cure overnight at room temperature.

Images were acquired using a Zeiss LSM980 confocal microscope, using either a 20× or 63× oil immersion objective. DFHBI-1T was visualized through EGFP filter with shortened detection range (490–552 nm) to reduce mCherry bleed through. Image processing and analysis were performed using ZEN Blue (Zeiss) or ImageJ (NIH) software.

Quantitative PCR

Total RNA was extracted using TriPure Isolation Reagent (Roche) according to the manufacturer's protocol. RNA concentration was measured using a QuickDrop spectrophotometer (Molecular Devices), and 1 µg of total RNA was used to synthesize cDNA using the LunaScript RT SuperMix Kit (New England Biolabs). cDNA was subsequently diluted 1:10 in TE buffer.

qPCR was performed using Luna Universal qPCR Master Mix (NEB) on a CFX384 Touch Real-Time PCR Detection System (Bio-Rad). Each 10 µL reaction contained 5 µL of Luna Master Mix, 1 µL of diluted cDNA, and 250 nM of each primer.

Gene expression was quantified using the ΔΔCt method, normalized to Gapdh, and reported as fold change relative to the control vector. All reactions were performed in at least three technical replicates, and error bars are presented as SEM.

Transmission electron microscopy

Cultured cells were collected by sedimentation, and the resultant pellets were fixed using 2.5% glutaraldehyde and 2.0% paraformaldehyde in 0.1 M Sodium Cacodylate buffer. After fixation, pellets were post-fixed in 1% osmium tetroxide, and block stained in 1% aqueous uranyl acetate, followed by dehydration and embedding in Embed812 resin (Electron Microscopy Sciences). Ultrathin sections were cut, collected on copper grids, and post-stained using uranyl acetate followed by Reynolds' lead citrate solution. Images were acquired using a Thermo Fisher FEI Tecnai 12 BioTwin Transmission Electron Microscope (Thermo Fisher Scientific) equipped with a Gatan OneView CMOS (4 K by 4 K) camera (Gatan). Image processing and analysis were performed using Gatan Digital Micrograph or ImageJ software.

Reporting summary

Further information on research design is available in the Nature Portfolio Reporting Summary linked to this article.

Data availability

The data supporting the findings of this study are available within the main text and its Supplementary Information. The raw data and statistical analysis of fluorescence intensity in this study are provided in the Source Data files. Any additional requests for information can be directed to, and will be fulfilled by, the corresponding authors. Source data are provided with this paper.

References

1. Henninger, J. E. & Young, R. A. An RNA-centric view of transcription and genome organization. *Mol. Cell* **84**, 3627–3643 (2024).
2. Guo, C. J., Xu, G. & Chen, L. L. Mechanisms of long noncoding RNA nuclear retention. *Trends Biochem Sci.* **45**, 947–960 (2020).
3. Khan, M., Hou, S., Chen, M. & Lei, H. Mechanisms of RNA export and nuclear retention. *Wiley Interdiscip. Rev. RNA* **14**, e1755 (2023).
4. Geary, C., Rothemund, P. W. K. & Andersen, E. S. A single-stranded architecture for cotranscriptional folding of RNA nanostructures. *Science* **345**, 799–804 (2014).
5. Geary, C., Grossi, G., McRae, E. K. S., Rothemund, P. W. K. & Andersen, E. S. RNA origami design tools enable cotranscriptional folding of kilobase-sized nanoscaffolds. *Nat. Chem.* **13**, 549–558 (2021).
6. Tran, M. P. et al. Genetic encoding and expression of RNA origami cytoskeletons in synthetic cells. *Nat. Nanotech*. **20**, 664–671 (2025).
7. Liu, D. et al. Branched kissing loops for the construction of diverse RNA homooligomeric nanostructures. *Nat. Chem.* **12**, 249–259 (2020).
8. Li, M. et al. In vivo production of RNA nanostructures via programmed folding of single-stranded RNAs. *Nat. Commun.* **9**, 2196 (2018).
9. Jepsen, M. D. E. et al. Development of a genetically encodable FRET system using fluorescent RNA aptamers. *Nat. Commun.* **9**, 18 (2018).
10. Nguyen, M. T. A., Pothoulakis, G. & Andersen, E. S. Synthetic translational regulation by protein-binding RNA origami scaffolds. *ACS Synth. Biol.* **11**, 1710–1718 (2022).
11. Pothoulakis, G., Nguyen, M. T. A. & Andersen, E. bbeS. Utilizing RNA origami scaffolds in Saccharomyces cerevisiae for dCas9-mediated transcriptional control. *Nucleic Acids Res.* **50**, 7176–7187 (2022).
12. Zhang, T. et al. Programmable in vitro and in vivo folding of single-stranded nucleic-acid wireframe origami. *Chem* **10**, 2550–2563 (2024).
13. Fu, T. J. & Seeman, N. C. DNA double-crossover molecules. *Biochemistry* **32**, 3211–3220 (1993).
14. Shen, Z. Y., Yan, H., Wang, T. & Seeman, N. C. Paranemic crossover DNA: a generalized Holliday structure with applications in nanotechnology. *J. Am. Chem. Soc.* **126**, 1666–1674 (2004).
15. Afonin, K. A., Cieply, D. J. & Leontis, N. B. Specific RNA self-assembly with minimal paranemic motifs. *J. Am. Chem. Soc.* **130**, 93–102 (2007).
16. Han, D. et al. Single-stranded DNA and RNA origami. *Science* **358**, eaao2648 (2017).
17. Qi, X. et al. Programming molecular topologies from single-stranded nucleic acids. *Nat. Commun.* **9**, 4579 (2018).
18. Sampedro Vallina, N., McRae, E. K. S., Geary, C. & Andersen, E. S. An RNA paranemic crossover triangle as A 3D module for cotranscriptional nanoassembly. *Small* **19**, e2204651 (2022).
19. Dietz, H., Douglas, S. M. & Shih, W. M. Folding DNA into twisted and curved nanoscale shapes. *Science* **325**, 725–730 (2009).
20. Han, D. R. et al. DNA origami with complex curvatures in three-dimensional space. *Science* **332**, 342–346 (2011).

21. Horiya, S. et al. RNA LEGO: magnesium-dependent formation of specific RNA assemblies through kissing interactions. *Chem. Biol.* **10**, 645–654 (2003).
22. Qi, X. D. et al. RNA origami nanostructures for potent and safe anticancer immunotherapy. *Acs Nano* **14**, 4727–4740 (2020).
23. Filonov, G. S., Moon, J. D., Svensen, N. & Jaffrey, S. R. Broccoli: rapid selection of an RNA mimic of green fluorescent protein by fluorescence-based selection and directed evolution. *J. Am. Chem. Soc.* **136**, 16299–16308 (2014).
24. Ouellet, J. RNA fluorescence with light-up aptamers. *Front. Chem.* **4**, 29 (2016).
25. Byron, S. A., Van Keuren-Jensen, K. R., Engelthaler, D. M., Carpten, J. D. & Craig, D. W. Translating RNA sequencing into clinical diagnostics: opportunities and challenges. *Nat. Rev. Genet.* **17**, 257–271 (2016).
26. Zhu, Y., Zhu, L., Wang, X. & Jin, H. RNA-based therapeutics: an overview and prospectus. *Cell Death Dis.* **13**, 644 (2022).
27. Isermann, T., Sers, C., Der, C. J. & Papke, B. KRAS inhibitors: resistance drivers and combinatorial strategies. *Trends Cancer* **11**, 91–116 (2025).
28. Stickler, S., Rath, B. & Hamilton, G. Targeting KRAS in pancreatic cancer. *Oncol. Res.* **32**, 799–805 (2024).
29. Yang, Q. et al. Angle-controllable RNA tiles for programable array assembly and RNA sensing. *Nat. Commun.* **16**, 3728 (2025).
30. Rogers, T. A., Andrews, G. E., Jaeger, L. & Grabow, W. W. Fluorescent monitoring of RNA assembly and processing using the split-spinach aptamer. *ACS Synth. Biol.* **4**, 162–166 (2014).
31. Alam, K. K., Tawiah, K. D., Lichte, M. F., Porciani, D. & Burke, D. H. A fluorescent split aptamer for visualizing RNA–RNA assembly in vivo. *ACS Synth. Biol.* **6**, 1710–1721 (2017).
32. Schonborn, J. et al. Monoclonal antibodies to double-stranded RNA as probes of RNA structure in crude nucleic acid extracts. *Nucleic Acids Res.* **19**, 2993–3000 (1991).
33. Weber, F., Wagner, V., Rasmussen, S. B., Hartmann, R. & Paludan, S. R. Double-stranded RNA is produced by positive-strand RNA viruses and DNA viruses but not in detectable amounts by negative-strand RNA viruses. *J. Virol.* **80**, 5059–5064 (2006).
34. Li, X., Kim, H., Litke, J. L., Wu, J. & Jaffrey, S. R. Fluorophore-promoted RNA folding and photostability enables imaging of single broccoli-tagged mRNAs in live mammalian cells. *Angew. Chem. Int. Ed. Engl.* **59**, 4511–4518 (2020).
35. Katahira, J. Nuclear export of messenger RNA. *Genes* **6**, 163–184 (2015).
36. Song, Z., Lin, J., Li, Z. & Huang, C. The nuclear functions of long noncoding RNAs come into focus. *Noncod. RNA Res.* **6**, 70–79 (2021).
37. Herman, A. B., Tsitsipatis, D. & Gorospe, M. Integrated lncRNA function upon genomic and epigenomic regulation. *Mol. Cell* **82**, 2252–2266 (2022).
38. Shokrollahi, M. & Mekhail, K. Interphase microtubules in nuclear organization and genome maintenance. *Trends Cell Biol.* **31**, 721–731 (2021).
39. van Steensel, B. & Belmont, A. S. Lamina-associated domains: links with chromosome architecture, heterochromatin, and gene repression. *Cell* **169**, 780–791 (2017).
40. Williams, S. et al. in *DNA Computing*. (eds. A. Goel, F. C. Simmel & P. Sosík) 90-101 (Springer Berlin Heidelberg, 2009).
41. Ennifar, E., Walter, P., Ehresmann, B., Ehresmann, C. & Dumas, P. Crystal structures of coaxially stacked kissing complexes of the HIV-1 RNA dimerization initiation site. *Nat. Struct. Biol.* **8**, 1064–1068 (2001).
42. Lee, A. J. & Crothers, D. M. The solution structure of an RNA loop–loop complex: the ColE1 inverted loop sequence. *Structure* **6**, 993–1007 (1998).
43. Goddard, T. D. et al. UCSF ChimeraX: meeting modern challenges in visualization and analysis. *Protein Sci.* **27**, 14–25 (2018).
44. Zadeh, J. N. et al. NUPACK: analysis and design of nucleic acid systems. *J. Comput. Chem.* **32**, 170–173 (2011).
45. Zuker, M. Mfold web server for nucleic acid folding and hybridization prediction. *Nucleic Acids Res.* **31**, 3406–3415 (2003).

Acknowledgements

This work is supported by US National Science Foundation (NSF) grants (CCF-2007821) and (DMR-2046835), and a faculty Startup Fund from Rutgers University to F.Z., and the National Institute of Health (NIH) grants R01DK139790 and R21AI167079, and faculty Startup Funds from Rutgers University to J-P.E. We acknowledge the electron microscopy facilities of the Department of Biological Sciences, Laboratory for Advanced Imaging, and Rutgers School of Public Health Core Imaging Laboratory.

Author contributions

F.Z. and H.Y. conceived the original idea. X.C. and F.Z. designed the structures. X.C. assigned the sequences, characterized the formation of single-stranded RNA nanostructures, and integrated light-up aptamers into the structures. Q.Y. performed the experiments for RNA sensing in vitro. M.J. and J-P.E. developed the expression constructs, transfection protocols in human cells, and projected the biological applications for the nanostructures. M.J. and E.M.B. conducted the TEM characterization and M.J completed the confocal imaging studies. The manuscript was written through the contributions of all authors. All authors have given approval to the final version of the manuscript.

Competing interests

F.Z., J-P.E., X.C., and M.J. have filed a provisional US patent based on this work. The remaining authors declare no competing interests.

Additional information

Supplementary information The online version contains supplementary material available at https://doi.org/10.1038/s41467-025-67817-y.

Correspondence and requests for materials should be addressed to Jean-Pierre Etchegaray or Fei Zhang.

Peer review information *Nature Communications* thanks Ebbe Andersen, Bryan Wei, Cody Geary and the other anonymous reviewer for their contribution to the peer review of this work. [A peer review file is available].